International Journal of Heat and Mass Transfer 143 (2019) 118471

Contents lists available at ScienceDirect

International Journal of Heat and Mass Transfer

journal homepage: www.elsevier.com/locate/ijhmt

Temperature-dependent infrared optical and radiative properties of platinum

J. Orosco, C.F.M. Coimbra *

Department of Mechanical and Aerospace Engineering, Center for Energy Research, University of California San Diego, La Jolla, CA 92093-0411, United States

ARTICLE INFO

Article history:
Received 27 April 2019
Received in revised form 17 July 2019
Accepted 22 July 2019

Keywords:
Optical properties
Radiative properties
Metals
Varshni equation
Resistivity
Kramers-Kronig relations

ABSTRACT

We propose a spectral thermophysical model for the infrared optical and radiative properties of metals. The model is suitable for metals possessing nontrivial valency and interband dynamics activated at infrared wavelengths, and consists of an anomalous intraband component and a Gaussian-Lorentzian interband component. The utility of the model is demonstrated by application to platinum, a material of technical importance that also possesses the relevant intra- and interband characteristics. The model yields accurate estimates of the temperature-dependent spectral directional radiative properties over the wavelength range from 1.5 to 16 μm, and the temperature range from 0 to 1400 K. Results indicate that when computing the total normal, directional, or hemispherical properties, the model can be used for accurate extrapolation over the entire Planck-weighted spectrum. High-fidelity reproduction of the directional properties validates the inverse extrapolated estimates of the complex-refractive index. This indicates that the model can be interfaced with alternative Fresnel frameworks, such as those used to characterize surfaces that have been systematically or randomly roughened. A MATLAB code is provided as supplemental material for reproducibility and convenient implementation of the model.

1. Introduction

When subject to incident electromagnetic radiation, a solid medium will respond in accordance with its atomic composition and structure. The systematic characterization of this response as a function of the material composition and structure is expressed in terms of the optical properties of the medium. These properties are generally complex-valued quantities—such as the conductivity or refractive index—that provide a constitutive basis for the governing Maxwell-Heaviside equations. When coupled with the theory of Fresnel, the optical properties can be used to compute the real-valued surface radiative properties. The latter characterize the radiant exchange of energy at relevant interfaces between media. The ability to form accurate predictions about the behaviors of electromagnetic systems under differing conditions relies critically on accurate knowledge of the optical and radiative properties of the interacting media. Such predictions may be desirable from a purely theoretical standpoint, or may be necessary to satisfy the demands of design-driven applications. Thus, theoretician and engineer alike benefit from the functionality of models that reliably explain the observed responses.

In many practical scenarios, the interaction of electromagnetic radiation with metals depends heavily on the material response to infrared radiative forcing. This includes a broad class of applications that ranges from modeling the behaviors of nanoscale infrared antennas [1] to the design of metamaterials for purposes of signal privacy [2]. The infrared regime is particularly dominant when characterizing the radiant exchange of thermal energy, since this exchange is dependent on Planck's energy density distribution, which is densely weighted over infrared wavelengths at pre-transition temperatures of most common metals. In this setting, thermophysical descriptions of the relevant properties can be utilized for the design of engine componentry [3], for the implementation of non-invasive thermometry [4,5], and for the design of thermal systems [6].

When dealing with the purely intraband (*i.e.*, free-carrier) response of ideal media such as the monovalent noble metals, accurate models can be obtained by utilizing the simple model first introduced by Drude over a century ago [7]. However, the Drude model fails to completely explain the observed responses in many non-ideal scenarios [8–12]. This is typically the case, for example, when dealing with the complex valence configurations of transitions metals. The issue becomes further complicated when one seeks to characterize the associated thermophysical response. In a recent series of studies, we addressed this issue by deriving a

* Corresponding author.
E-mail address: ccoimbra@ucsd.edu (C.F.M. Coimbra).

https://doi.org/10.1016/j.ijheatmasstransfer.2019.118471
0017-9310/

model for anomalous intraband dynamics [13], and then extending its use for thermophysical applications [14,15].

Still more difficulty is encountered when dealing with media involving interband mechanisms excited at infrared wavelengths, since these mechanisms—as a function of temperature—behave in a divergent and substantially more complicated manner than the simpler intraband mechanisms. Yet for the reasons previously noted, it is nonetheless desirable to characterize the thermophysical infrared responses of such media. In this work, we address this need and build upon our previous studies by introducing a thermophysical model for the optical and radiative properties of transition metals where the combined intraband and interband mechanisms play an important role in determining the infrared response. The utility of the model is demonstrated by applying it to platinum, a transition metal possessing nontrivial valency and infrared activated interband dynamics. Platinum is also a relevant choice due to its wide use in engineering applications [16–20].

The remainder of this work proceeds as follows. In Section 2 we present the relevant theory, including the definition of the anomalous intraband component in Section 2.1 and the definition of the interband component in Section 2.2. The model is applied to platinum in Section 3 and detailed attention is given to the systematic inclusion low-temperature measurements in Section 3.3. The results are presented in Section 4, which include results for peripheral properties (such as the DC resistivity) in Section 4.1 and results for the radiative properties (such as the spectral thermophysical emissivity) in Section 4.2. A brief concluding discussion of the main points of the paper is presented in Section 5. A MATLAB implementation of the model is provided as supplemental material.

2. Theory

The linear response of a metal when subject to incident electromagnetic radiation can be characterized in terms of its optical properties (*e.g.*, impedance), which take the form of complex-valued multivariate functions of wavelength and temperature. A typical approach to modeling these properties is to express, at microscale, the motions of the relevant particles [15]. For metallic conductors, this approach consists largely of describing the intraband (free) and interband (bound) electron dynamics. A macroscopic model can then be obtained from the ensemble average of the microscopic equations of motion. The complex-valued properties are then obtained under a Fourier transform of the macroscopic equations.

The (electric) susceptibility $\chi \in \mathbb{C}$ is a fundamental intuitive example characterizing the positional response, and is obtained as the Fourier transform of the bulk polarization density. One may write a high-level expression for the susceptibility:

$$\chi(\lambda,T) = \sum_{\phi} \chi_{\phi}(\lambda,T) + \sum_{\beta} \chi(\lambda,T), \tag{1}$$

where χ_{ϕ} and χ_{β} are the intra- and interband contributions, respectively. When intraband dynamics are the modeling focus, and if there is sufficient decoupling between the intra- and interband regimes, one can reasonably take the approximation $\sum \chi_{\beta} = \text{constant} \in \mathbb{R}$ [15]. This is frequently the case when considering electromagnetic forcing at infrared wavelengths, since this spectral band approximately aligns with the intraband regime for many metals. In some cases, however, there is insufficient temporal decoupling between these dynamical regimes and one must explicitly model the bound-state contribution to the overall response. The infrared response of elemental platinum—which serves as the modeling focus of the present study—is such an instance. For the reader's benefit, we give attention to each of these model components independently so that their contribution to the total model may be more fully understood.

2.1. Intraband model component

In a recent series of studies, we have derived a fixed-temperature anomalous free-carrier transport model [13] and described a consistent method of extending its use for the purposes of thermophysical modeling [15]. In the time domain, the macroscopic model is expressed in terms of fractional differential transport equations at time t and temperature T:

$$\tau_c(T)\,\frac{dj_d(t)}{dt} + j_d(t) = \frac{n_d e^2}{m^*}\,\tau_c(T)\,E(t), \tag{2a}$$

$$\tau_a(T)\,\frac{dj_a(t)}{dt} + j_a(t) = \frac{n_d e^2}{m^*}\,\tau_a(T)\,\tau_f^{\mu}\,\frac{d^{\mu}E(t)}{dt^{\mu}}, \tag{2b}$$

subject to the physical constraint $\tau_a = \psi(T)\,\tau_c$, where ψ is a dimensionless scaling parameter. The equations describe the evolution of the current density $j = j_d + j_a$ in response to the electric field E as the sum of contributions from a semiclassical component (2a) and an anomalous component (2b). The parameters of the model are: characteristic scattering rate, $1/\tau_c$; characteristic time of field disorder relaxation, τ_f; electronic number density, n_d; and effective mass, m^*. Here the elementary charge is denoted e. Units are SI throughout. The fractional differential component on the right-hand side of (2b) expresses a non-Markovian field relaxation having a memory decay intensity characterized by the parameter μ.

The foregoing current density equations lead to an intraband susceptibility model:

$$\chi_{\phi}(\lambda,T) = \chi_d(\lambda,T) + \chi_a(\lambda), \tag{3}$$

where

$$\chi_d(\lambda,T) = -\frac{\lambda^2\,\sigma_0(T)}{2\pi c_0\,\varepsilon_0}\left(\frac{f_{\phi}}{i\lambda + \lambda_c(T)}\right) \tag{4}$$

is a Drude component with oscillator strength f_{ϕ}, and the anomalous component is

$$\chi_a(\lambda) = -(-i)^{\mu}\,\frac{\lambda^2\,\sigma_a}{2\pi c_0\,\varepsilon_0}\left(\frac{\lambda_f}{\lambda}\right)^{\mu}\left(\frac{f_{\phi}}{i\lambda + \lambda_a}\right). \tag{5}$$

Due to its origin in a fractional differential equation, the anomalous term has the property that it partitions the energy between absorptive and dispersive components of the response model. The energy partitioning property of fractional and variable order operators has been investigated in detail [21]. In all cases, characteristic periods have been converted to characteristic wavelengths by defining a relation of the type $\lambda_c = \tau_c/2\pi c_0$. We have further defined the long-wavelength (*i.e.*, DC) conductivity:

$$\sigma_0(T) = \frac{n_d e^2}{m^*}\,\tau_c(T), \tag{6}$$

as well as its anomalous counterpart

$$\sigma_a = \frac{n_d e^2}{m^*}\,\psi(T)\,\tau_c(T) = \psi(T)\,\sigma_0(T) = \text{constant}. \tag{7}$$

The temperature independence of the anomalous component derives from a model-reductive, purely empirical result in our earlier studies [14,15]. The parameter ψ acts as a time constant modifier for a single effective carrier type that may experience a different collisional rate in independent regimes (*i.e.*, when $\psi = 1$, the Eqs. (2) collapse into a single expression). This implies the physical model constraints:

$$\frac{\sigma_a}{\lambda_a} = \frac{\sigma_0(T)}{\lambda_c(T)} = \frac{n_d e^2}{m^*} \equiv \kappa = \text{constant}. \tag{8}$$

Actually, the quantity in (8) depends on temperature through the coefficient of thermal expansion—this can be accounted for, if so desired, by explicitly fixing the variation in accordance with the literature. For the sake of simplicity, we omit this here since the variation resulting from these effects is negligible even over the temperature ranges investigated here ($\Delta T \approx 1400$ K). An otherwise freely varying thermal expansion term would represent a spurious degree of freedom in the model.

2.2. Interband model component

In a recent paper [22], Minissale and collaborators have investigated the potential for repurposing a temperature-dependent Lorentz harmonic oscillator for the description of interband behaviors in a thermophysical setting. The oscillator definition expands on earlier work by Yokozeki et al. [23] that investigates thermal effects on atomic stretching mode vibrations in ionic liquids. The wavelength-dependent form of the model is

$$\chi_l(\lambda, T; \lambda_n) = \frac{\lambda_p(T)^{-2} f_\beta}{\lambda_n(T)^{-2} - \lambda^{-2} - i\lambda^{-1}\lambda_\Gamma(T)^{-1}}, \tag{9}$$

which is expressed in terms of the temperature-dependent parameters

$$\lambda_p(T) = \lambda_{p,r}[1 + \alpha(\Theta_r - 1)]^{1/2}, \tag{10a}$$

$$\lambda_\Gamma(T) = [\lambda_{\Gamma,r}^{-1} + \gamma(\sqrt{\Theta_r} - 1)]^{-1}, \tag{10b}$$

$$\lambda_n(T) = [\lambda_{n,r}^{-1} - \nu(\Theta_r - 1)]^{-1}, \tag{10c}$$

where $\Theta_r = T/T_r$ for reference temperature T_r, the expression $(\cdot)_{x,r}$ denotes the parameter value $(\cdot)_x$ at $T = T_r$, α is the coefficient of thermal expansion, and $\gamma > 0$ and $\nu > 0$ are empirical material constants derived on the basis of the liquid state physics hard sphere model (see supplemental material in [23]). As noted previously, one can safely take λ_p as constant due to the negligible effect of thermal expansion over the investigated temperature range.

In fact, the temperature dependence of the resonant wavelength we have given in (10c) is very different from that described in Ref. [22]. The model in that study is based on a $T^{1/2}$ proportionality (of the *square* of the resonant frequency) that was derived by first assuming the $T^{1/2}$ damping proportionality derived by Yokozeki in [23], and then using a dimensional argument constrained by the denominator of the Lorentz model to arrive at the result. Such a derivation assumes that the temperature dependences of these two parameters are coupled through the "correctness" of the Lorentz model, an argument that we find to be conceptually dubious. In fact, the processes that lead to the thermoderivatives of these parameters—or, more aptly, of the dynamics that they represent—may consist of substantially independent components [24]. For this reason, we prefer the proportionalities originally derived by Yokozeki for *both* λ_Γ and λ_n, which we have given in (10b) and (10c), respectively. It is also worth noting that for $T \gg T_D$ (T_D is the Debye temperature), such a linear proportionality has been derived and observed for band gaps in semiconductors [25], as well as for the absorption edges in, *e.g.*, the monovalent noble metals [24]. When $T \ll T_D$, the circumstances become more complicated and we must account for this in the model as described in a later section.

A typical approach to modeling bound state susceptibility contributions (for both conductive and dielectric media) is to superpose as many basis oscillators as may be necessary to sufficiently reproduce the experimental observations. This can, however, lead to the implementation of unphysical oscillator components and often these may have unrealistic attributes (*e.g.*, a collisional rate that far exceeds the resonant frequency). Furthermore, it has been observed that in some media a Lorentzian profile is not capable of fully explaining the data and a Gaussian-Lorentzian interpolated profile is more appropriate. This reasoning can be understood by considering, for example, the semi-stochastic lattice disorder in amorphous dielectrics, which tends to have a smoothing effect on the Lorentzian line shape otherwise observed in the associated crystalline form. Examples of these behaviors in amorphous dielectrics were first noted in [26] and have been more recently studied in the works of, *e.g.*, [27,28]. In the case of metals, examples of these behaviors have been empirically demonstrated in a number of studies. Some recent examples include efforts at modeling the Gauss-Lorentz character of surface plasmon resonance structures [29,30] in elemental metals. Cubic metals, which are well-known to have a spherical index ellipsoid, are optically isotropic, so that these behaviors will be present in both monocrystalline and (randomly oriented) polycrystalline samples.

A widely adopted approach to addressing these issues is based on the discrete-to-continuous oscillator sum substitution

$$\chi_{ek}(\lambda) = \sum_\beta \chi_\beta(\lambda) \to \int_{-\infty}^{\infty} \mathcal{K}_g(y - \lambda_n)\, \chi_l(\lambda; y)\, dy, \tag{11}$$

where

$$\mathcal{K}_g(\lambda_n) = \frac{\lambda_\sigma}{\sqrt{2\pi}} \exp\left[-\left(\frac{\lambda_\sigma}{\sqrt{2}\lambda_n}\right)\right], \tag{12}$$

is a Gaussian smoothing kernel that applies an amplitude correction to the fixed-temperature Lorentz model $\chi_l(\lambda; \lambda_n)$ about the resonant mode. The Gaussian wavelength λ_σ is associated (in the solid state setting) with lattice disorder.

To the knowledge of the authors, the first appearance of the convolution (11) is in the works of Efimov and Khitrov [26]. Over a decade later, Brendel and Bormann [27] provided a closed-form approximation of the convolution based on a well-known domain-restricted (to the right-half complex plane) result given by Abramowitz and Stegun [31]. Their result—which has come to be known as the Brendel-Bormann oscillator—was later refined in terms of the Faddeeva function by Rakić and coworkers [32]. Unfortunately, the Brendel-Bormann oscillator—contrary to the statements made in [27,32]—fails to satisfy two important criteria imposed by the Kramers–Kronig relations: Hermicity (due to the domain restricted evaluation) and upper half-plane holomorphism (due to a singularity in the leading fractional factor). As it turns out, the convolution model (11) originally given by Efimov and Khitrov is always non-causal and we have provided a proof for this in Appendix A.

The aforementioned issues have been examined at length in our earlier study [33], where we have derived an alternative approximation to (11). Our derivation is based on an analytic continuation of the Abramowitz and Stegun result into the left-half plane (thus retaining Hermicity) along with a functional decomposition that permits singularity removal (thus retaining upper half-plane analyticity). Our model therefore strictly satisfies the Kramers-Kronig relations. Furthermore, this improved approximation of the convolution ensures that, for bound oscillators with small damping, the spectral coordinate of the maximum of the absorption profile remains in agreement with the resonant parameter λ_n even as the profile is made increasingly Gaussian (this is not so for the Brendel-Bormann model). We refer to our model as the Gauss-Lorentz oscillator (GLO).

For the problem at hand, we generalize our earlier fixed-temperature GLO by incorporating the temperature-dependent Lorentz oscillator definition. This leads to the definition

$$\chi_\beta(\lambda, T) = \mathcal{A}(T)\, \mathcal{S}(\lambda, T), \tag{13}$$

where the dimensionless shape function has the property $\mathcal{S}(\infty,T)=1$ so that $\chi_\beta(\infty,T)=\mathcal{A}(T)=\lambda_n(T)^2 f_\beta/\lambda_p(T)^2$, which is in exact agreement with the Lorentz oscillator. The shape function is

$$\mathcal{S}(\lambda,T)=\left(\frac{s_w[z_+(\lambda,T)]+s_w[z_-(\lambda,T)]}{\chi_\infty(T)}\right), \tag{14}$$

where

$$s_w(z)=i\pi w(z)+\exp(-z^2)\left[\log(z)+\log\left(-\frac{z^*}{|z|^2}\right)-i\pi\right], \tag{15}$$

contains the previously noted analytic continuation (the second term on the right-hand side). Here $\log(\cdot)$ is the complex logarithm, z^* is the complex conjugate of z, $|z|=\sqrt{zz^*}$, and $z_\pm(\lambda,T)=[\pm\zeta(\lambda,T)-\lambda_n(T)^{-1}]/\sqrt{2}\,\lambda_\sigma^{-1}$, with $\zeta(\lambda,T)=\zeta'(\lambda,T)+i\zeta''(\lambda,T)$:

$$\zeta'(\lambda,T)=\left(\frac{[\lambda^{-2}+\lambda_\Gamma(T)^{-2}]^{1/2}+\lambda^{-1}}{2\lambda}\right)^{1/2}, \tag{16a}$$

$$\zeta''(\lambda,T)=\left(\frac{[\lambda^{-2}+\lambda_\Gamma(T)^{-2}]^{1/2}-\lambda^{-1}}{2\lambda}\right)^{1/2}+\delta, \tag{16b}$$

and with δ being an arbitrary small real constant $0<\delta\ll 1$. In (14), the real-valued normalization parameter is

$$\chi_\infty(T)=-4\sqrt{\pi}D\left(-\frac{\lambda_\sigma}{\sqrt{2}\,\lambda_n(T)}\right). \tag{17}$$

The function $w(z)=\exp(-z^2)\operatorname{erfc}(z)$ in (15) is Faddeeva's function. It is related to Dawson's function $D(x)=(\sqrt{\pi}/2)\exp(-x^2)\operatorname{erfi}(x)$ in (17) as $D(x)=(\sqrt{\pi}/2)\,\mathbb{I}\mathrm{m}\{w(x)\}$ for $x\in\mathbb{R}$.

It is of critical importance to note that, despite its complicated appearance, the preceding GLO definition adds only one additional parameter to the underlying Lorentz model, and that this parameter is temperature-independent. This means that the fidelity and robustness of the GLO is realized without adding additional complication to the regression procedure for the temperature-dependent parameters.

The real and imaginary parts of the GLO for positive and negative wavelengths have been plotted in Fig. 1. The odd (even) character of the imaginary (real) parts at all T illustrates the Hermicity. A gray colored trace has been added to the surface of the absorption profile that indicates the position of the profile maximum at any temperature. As the temperature is increased, the absorption peak is damped and shifted, so that the integrated absorption (*i.e.*, the area under $\mathbb{I}\mathrm{m}\{\chi_\beta\}$) is more strongly weighted toward longer wavelengths.

A final important detail should be noted regarding the GLO definition. If computed as written, expressions (16) are undefined at $\lambda=0$. However, the limiting behavior of (16) in (15) is such that $\lim_{\lambda\uparrow 0}\mathcal{S}(\lambda,T)=\lim_{\lambda\downarrow 0}\mathcal{S}(\lambda,T)=0$, which is readily verified by inspection of the profile behaviors about $\lambda=0$ in Fig. 1. Physically, this is consistent with the fact that at arbitrarily large forcing frequencies, the inertial response of the system diminishes asymptotically. Furthermore, since $\lim_{\lambda\to 0}\hbar\omega\Rightarrow E\to\infty$, we observe that the model remains well defined for all meaningful inputs.

2.2.1. Efficient computation of the dispersion integrals

The dispersion integrals (*i.e.*, Faddeeva's and Dawson's functions) are composite functions involving the complex-valued Gaussian exponential and complex-valued error functions. Due to the complications that arise when numerically evaluating these integrals, attempting their computation by direct composition in the native computing environment can lead to inaccuracies. In lieu of this method, we suggest the excellent suite of functions provided by Johnson [34], which have been implemented in C++ and have wrappers for common syntaxes (*e.g.*, MATLAB, Python, R, and Julia).

3. Application to platinum

The foregoing intra- and interband modeling components are combined in this section in order to arrive at a model for the infrared optical and radiative properties of platinum. This is achieved in terms of (1) with one intraband term and one interband term, modeled as (3) and (13), respectively.

Despite platinum's wide use in a number of applied contexts, there appears to be a sparse availability of models for describing its spectral thermophysical optical and radiative properties in the infrared regime. One reason for this is due to the complication of

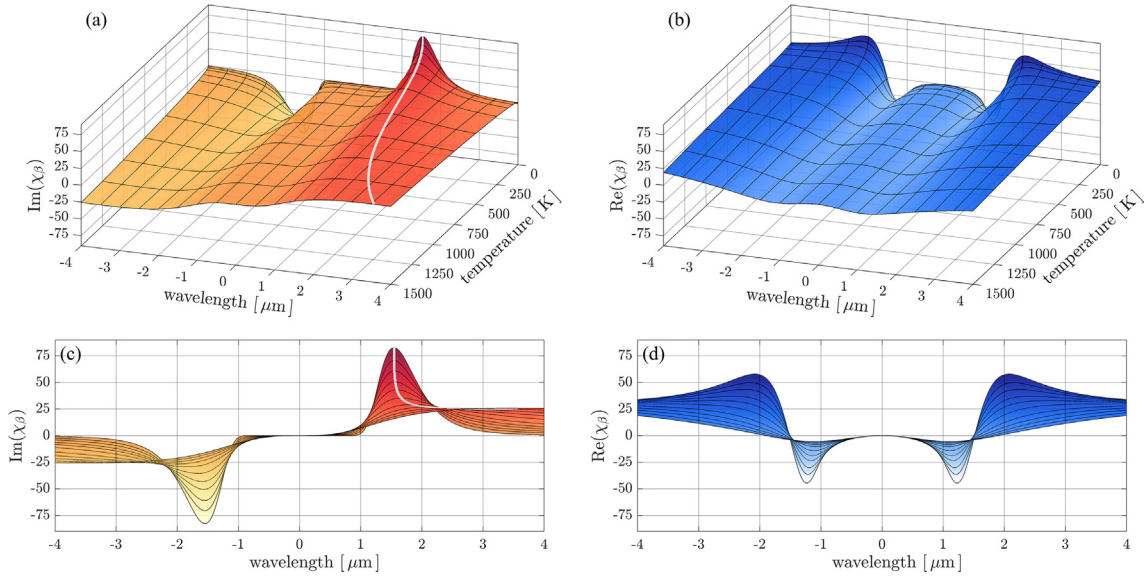

Fig. 1. The imaginary [(a) and (c)] and real [(b) and (d)] parts of the temperature-dependent Gauss-Lorentz oscillator defined in (13)–(17). The Hermicity of the model is observed at all temperatures. The gray trace along the surface in (a) and (c) indicates the change in wavelength of the profile maximum as a function of temperature. In (c), it is made evident that at higher temperatures the absorption peak is damped and absorption is dispersed over longer wavelengths.

modeling the interband mechanism governing these properties in the NIR portion of the spectrum. It is for these reasons that platinum was selected as the subject of the modeling efforts undertaken in this section.

The data used for this purpose represents thick media that is optically smooth over the infrared regime. The data were taken from four studies [35–38] and span eight temperatures $T \in \{4, 294, 306, 556, 583, 722, 833, 1424\}$ K.

3.1. Procedural regression of the model parameters

Due to the (initially) large number of degrees of freedom in the model, many of which vary with temperature, it is desirable to establish a systematic means for realizing the model from experimental data. Doing so will help to mitigate unnecessary parametric uncertainty that might otherwise be introduced. The method we outline here for achieving this goal is designed to reduce, as much as possible, the number of degrees of modeling freedom in each successive step. The steps are as follows: (i) regress and then fix the temperature-independent parameters at a relevant reference temperature, (ii) with the temperature-dependent parameters as the only free parameters, regress an independent set for each separate temperature defined by the data, and (iii) determine the remaining material functions (of temperature) from the resulting pairings of temperature and parameter value.

For gently varying spectral line shapes—such as those exhibited by most metals in the infrared regime—the line shape complexity will tend to have an inverse relationship with temperature due to the smoothing effect imposed by temperature-dependent lattice excitations. With this in mind, the reference temperature in (i) should be chosen as the lowest temperature made available by the data. Engaging the full modeling degrees of freedom in this way will help to reduce complications associated with determining the thermophysical parameters, while also subverting a potential source of parametric uncertainty.

3.2. Temperature-dependent resistivity

Since thermal expansion effects play a negligible role within the context of this study—inducing only about half of a percent change in the electron number density over the full range $\Delta T = 1420$ K—the constraint Eq. (8) implies that the intraband model component only involves a single material function of temperature. This is most appropriately expressed as the temperature-dependent resistivity, which has the form

$$\rho(T) = \rho_0 + \rho_i(T), \tag{18}$$

with ρ_0 representing the residual resistivity found in real materials due to lattice defects and where ρ_i arises due to thermally-induced interactions between electrons and electrons, or between electrons and phonons. This can be expressed in terms of a generalized Bloch-Grüneisen expression [39]:

$$\rho_i(T) = A\left(\frac{T}{T_D}\right)^n \int_0^{T_D/T} \frac{x^n e^x}{(e^x - 1)^2}\, dx, \tag{19}$$

where T_D is the Debye temperature, A is an interaction coupling constant, and the scattering index is such that: $n = 5$ if electron-phonon scattering is dominant, as is the case for simple metals; $n = 3$ when there is high probability of s-d band transitions, which is typical of transition metals; and $n = 2$ when electron-electron interactions dominate. At finite wavelengths, the latter of these effects is augmented by a factor carrying an inverse quadratic dependence on the product of wavelength and temperature [40].

For many metals, (19) can be accurately represented at pre-transition temperatures greater than T_D by the simple power-law relation [41]

$$\rho_i(T) = \rho_r \Theta_r^k, \tag{20}$$

where ρ_r is the resistivity at a given reference temperature and with Θ_r retaining its earlier definition.

3.3. Inclusion of low-temperature measurements

We have admitted into our modeling endeavor the helium-temperature measurements of Weaver [38]. Some adjustment to the model is necessary in order to account for the trend disparity that often accompanies measurements of metallic properties taken at room temperature and above versus those taken at temperatures much less than T_D. We give attention to two such (independent from one another) modifications presently.

3.3.1. Resistivity at low temperatures

The temperature-dependent resistivity expressed in (19) is such that $\rho_i \propto T^n$ ($n \geqslant 3$ for the scattering mechanisms listed above) when $T \ll T_D$ and $\rho_i \propto T$ when $T \gg T_D$. This represents an obstacle where the power-law model of (20) is concerned, since we are including data that is representative of both asymptotic regimes. We address this dilemma with the piecewise-power-law model definition:

$$\rho(T) = \begin{cases} \rho_l(T) & \Theta_r \leqslant 1 \\ \rho_h(T) & \Theta_r > 1 \end{cases}, \tag{21}$$

where $\rho_l(T) = \rho_0 + \rho_l \Theta_r^{k_l}$ and $\rho_h(T) = \rho_h \Theta_r^{k_h}$, and which we have found sufficient to describe the full range of the data. The number of degrees of freedom (DOFs) in (21) is made equivalent to the number of DOFs when using (18) with (20) by requiring that

$$\left.\frac{d^n \rho_l(T)}{dT^n}\right|_{T=T_r} = \left.\frac{d^n \rho_h(T)}{dT^n}\right|_{T=T_r} \text{ with } \quad n = \{0, 1\}, \tag{22}$$

which ensures first-order smoothness of the resistivity model at the reference temperature. The room temperature reference $T_r = 294$ K leads to a natural separation in the data, with the low-temperature resistivity equation being underdetermined. Since the low-temperature data (at $T = 4$ K) characterizes the residual resistivity, applying the constraints (22) then yields the remaining parameters:

$$\rho_l = \rho_h - \rho_0, \tag{23a}$$
$$k_l = k_h\,(\rho_h/\rho_l). \tag{23b}$$

The reader is directed to Fig. 2 in Section 4 for the illustrated results of this procedure.

3.3.2. Resonant wavelength at low temperatures

The second component of the model requiring our attention is the temperature-dependence of the resonant wavelength. At higher temperatures, the definition in (10c) is in agreement with asymptotic theoretical predictions [24]. It is therefore unsurprising that this definition sufficiently describes the measurements at higher temperatures. However, linear proportionality yields an increasingly poor description of the resonant wavelength temperature dependence at lower temperatures due to a shift in the dominant underlying mechanisms. This is expected, given that Yokozeki's derivation is intended to deal with atomic and molecular level interactions, and it therefore does not account for the temperature-dependence of electronic band structure.

In semiconductors, an appropriate analogue can be found in the temperature-dependence of the band gap. Theoretical treatments predict linear dependence at high temperatures and quadratic

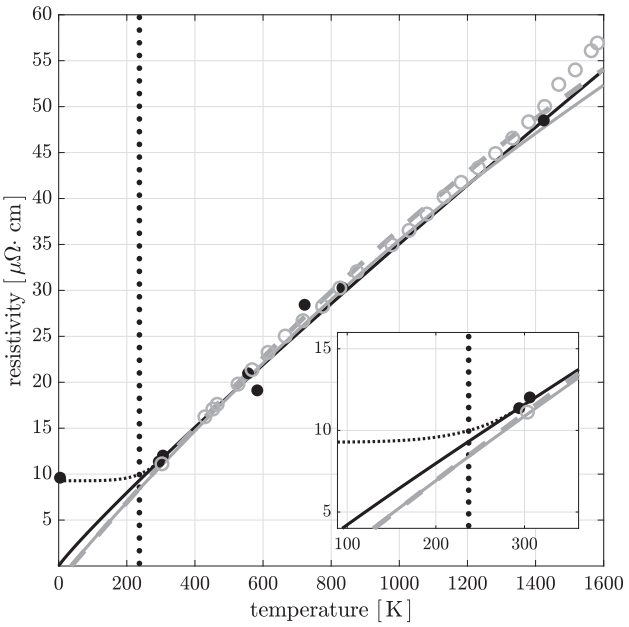

Fig. 2. Resistivity of platinum. Markers: independent fits of the proposed model at each temperature (black, filled) and recent measurements of Abadlia et al. [47] (grey, open). Lines: low-temperature (black, short-dashed) and high-temperature (black, solid) fits using the proposed model (21) with constraints (23) and parameters in Table 1, the fit of White [45] (grey, solid), and the fit of Wilthan et al. [46] (grey, long-dashed). The vertical dotted line indicates the Debye temperature of platinum, $T_D = 237$ K. In the presence of a residual resistivity, the onset of curvature occurs about $T \approx T_D$. The inset provides a "zoomed-in" view of the first-order smoothness joining the low- and high-temperature components of the model, as enforced by (22).

dependence at low temperatures [42]. This result lead Varshni to define his well known empirical relation for describing the broad-range band gap temperature dependence [25]. Although for metals there exists no band gap, one nonetheless observes similar dependencies in many of the critical structures defining the interband region, such as the profile maximum for a given absorption mode or the absorption edge of the medium. These dependencies have been empirically demonstrated and discussed in, for example, the historical works of Winsemius [24]. With this in mind, we define the (wavelength-dependent) generalization to Varshni's empirical relation:

$$\lambda_n(T) = \left(\lambda_n(0)^{-1} - \frac{\nu \Theta_r^{n+1}}{(\Theta_r + \theta)^n} \right)^{-1}, \tag{24}$$

where $\lambda_n(0)$ is the resonant wavelength at $T = 0$ K, and ν and θ are empirical material constants. In an idealized setting, θ should correspond approximately to the Debye temperature of the material, though Varshni found that this was rarely the case for semicondutors [25]. The generalized expression (24) recovers Varshni's original equation for $n = 1$. For $n > 1$, the high-temperature dependence of the increment term remains linearly proportional in accordance with theory and experiment [43]. However, the low-temperature dependence scales as T^{n+1}, providing flexibility for describing the more severe (*i.e.*, different from that of semiconductors) low-temperature asymptotics that may be observed in the critical structures defining the optical properties of metals. As described in the results section to follow, we obtain an excellent fit for $n = 1$ (*i.e.*, with Varshni's original equation), with θ corresponding to a "cutoff" temperature that is approximately equal to the Debye temperature.

4. Results

The main result of this paper is the susceptibility model obtained by combining (1), (3), and (13) with the accessory Eqs. (10), (21), and (24) under the constraints (8) and (23). When combined with Fresnel theory [44], one also obtains the optical indices and the directional surface radiative properties. In Table 1, we have listed the parameters representing the model realization when applied to the previously noted experimental platinum data. Ancillary results include: a DC resistivity model with tunable low-temperature asymptotics—and, with the use of the Wiedemann-Franz law, an estimate of the high-temperature thermal conductivity; and a model for the temperature dependence of the interband spectral coordinate. We have included in the supplemental material a MATLAB implementation of the model for the convenience of the user.

4.1. Peripheral properties

4.1.1. DC resistivity of platinum

In Fig. 2 we have plotted the resistivity values obtained by independently regressing a fixed-temperature model on each of the data sets, as described in Section 3. The resistivity model (21)—regressed on the independent values—is displayed in the same plot. Also shown: the resistivity fit of White [45], the fit of Wilthan et al. [46], and the recent measurements of Abadlia et al. [47]. Above $T_r = 294$ K, our resistivity model finds good agreement with the measurements of Abadlia et al. and the fit Wilthan et al., and excellent agreement with the fit of White.

Beyond the obvious implications for resistivity modeling, this also demonstrates the physical consistency of the more general proposed optical and radiative model, since it is possible to replace the proposed resistivity model with the noted expressions obtained in the literature from direct DC resistivity measurements and nonetheless obtain meaningful estimates for the optical and radiative properties. This is demonstrated in Appendix B. Although, it should be noted that the fits of White and Wilthan are obtained in ten DOFs and three DOFs respectively. The proposed resistivity model encompassing both low and high temperature regimes is obtained in three DOFs. Furthermore, since the model is defined in terms of the constraints (23), it is possible to "tune" the residual resistivity as desired—and as may be dictated by the medium, as in the case of Weaver's 4 K measurements—in order to obtain a variable low-temperature regime without affecting the

Table 1
Parameters for the susceptibility model obtained by combining (1), (3), and (13) with the accessory Eqs. (10), (21), and (24)) under the constraints (8) and (23). Any remaining parameters are obtained by using the aforementioned constraints with the associated values in this table. All resistivities are given in units of $\Omega \cdot \mu$m and all wavelengths are given in units of μm. The parameter κ, by definition, has units of μΩ/μm. All other parameters are dimensionless. All explicitly nondimensionalized parameters have been defined in terms of $\Theta_r = T/T_r$ with the room temperature reference $T_r = 294$ K. For the user's convenience, we have included MATLAB code that implements the model in the supplementary material.

Intraband								Interband							
ρ_0	ρ_h	k_h	ρ_a	λ_f	μ	f_ϕ	κ	λ_p	$\lambda_{\Gamma,r}$	γ	$\lambda_n(0)$	ν	θ	λ_σ	f_β
0.0928	0.1137	0.9197	3.9522	18.2500	0.0982	0.5800	0.4590	0.1293	2.4533	0.4012	1.5457	0.0365	0.8019	8.0450	0.1887

high-temperature fidelity. In the limit $\rho_0 \to 0$, the high-temperature curve is recovered by the low-temperature curve down to $T = 0$ K, with $\rho(T = 0) = 0$ for a perfect lattice. This is illustrated in Fig. 3.

4.1.2. Temperature-dependence of the interband spectral coordinate

The results of fitting the Varshni equation—expression (24) with $n = 1$—to the independently obtained resonant spectral coordinates of the temperature-dependent GLO (13) at each temperature have been plotted in Fig. 4. The dependent plot axis is given in units of inverse resonant wavelength (*i.e.*, proportional to $E = \hbar\omega$) so that a direct comparison can be made with the band gap fits typically found when fitting Varshni's expression [25]. Also shown: the best linear fit to the high-temperature region (corresponding to Yokozeki's model [23]) and the best fit of the model from Ref. [22] to the high-temperature region. Among the various important conclusions that can be extracted from the plot, perhaps the most immediate is the distinct separation into nonlinear (at lower temperatures) and linear (at higher temperatures) regimes. The central temperature for the transitional regime is, unsurprisingly, the Debye temperature: $T_D = 237$ K.

The parameter $\theta = 0.8019$ in the Varshni fit corresponds to the unnormalized temperature $T_\theta = 294\ \text{K} \cdot \theta \approx 236$ K, which—when coupled with the accuracy of the fit—implies a remarkable level of theoretical consistency. Inspection of the point-wise absolute relative residuals in the subplot makes it clear that there is roughly an order-of-magnitude difference between the models, with the Varshni fit yielding a substantial improvement over the other two models, even for $T > T_D$ and despite the fact that the other models were regressed explicitly on this region. The reason that the Varsni expression outperforms even the linear fit at higher temperatures is revealed by inspection of the inset: the "strictly" linear regime does not begin until $T \gtrsim 2 \cdot T_D$ (*i.e.*, $T \gg T_D$).

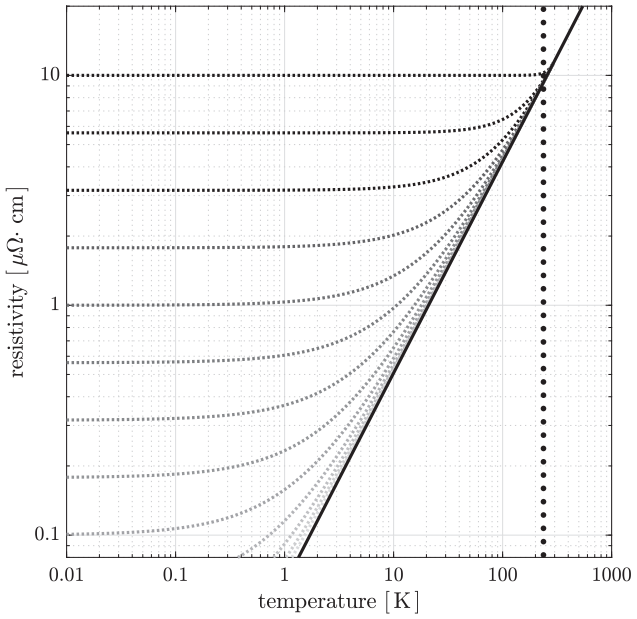

Fig. 3. Tunable low-temperature profile for the resistivity component of the proposed model. The high-temperature regime with $\Theta_r > 1$ (solid black line) is given by $\rho_h(T)$ in (20) and the low-temperature regime with $\Theta_r \leqslant 1$ (short-dashed lines) is given by $\rho_l(T)$, with increasing residual resistivity values (light to dark) on $\rho_0 \in [0.01, 10]$ μΩ·cm. The remaining parameters are determined with (23) by using the fixed parameters in Table 1. The vertical dotted line indicates the Debye temperature of platinum, $T = 237$ K. Continuity and smoothness about $\Theta_r = 1$ is enforced by the constraints (22), leading to a "tunable" low-temperature profile. When ρ_0 is set to zero, the low-temperature profile recovers the high-temperature profile down to $T = 0$ K, leading to $\rho(T = 0) = 0$ (*i.e.*, for a "perfect" lattice).

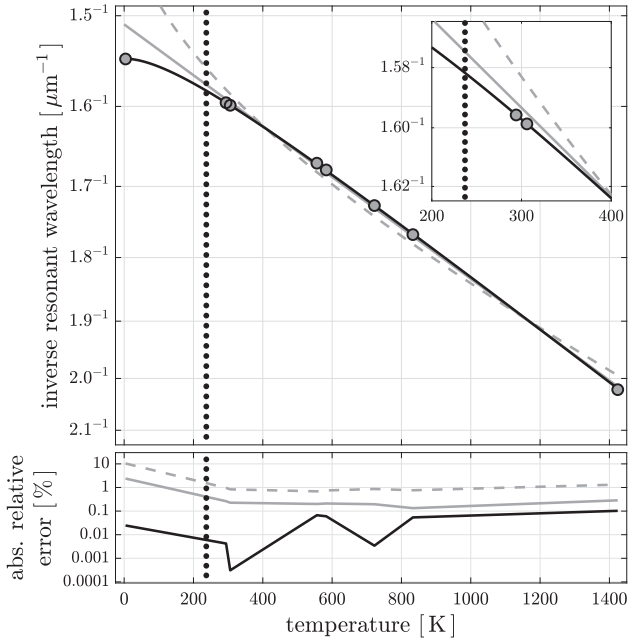

Fig. 4. Temperature dependence of the interband resonant wavelength. Lines: generalized Varshni expression (24) (solid, black), Yokozeki's model [23] (solid, grey), and Minissale's model [22] (dashed, grey). Markers indicate values obtained as described in Section 3.1. The vertical dotted line indicates the Debye temperature, $T_D = 237$ K. The residuals subplot indicates roughly order-of-magnitude separation between the goodness of fit of the models, with the Varshni-type equation providing the best fit. This is true for both the $T < T_D$ and the $T > T_D$ regimes since, as can be observed in the inset, departure from linearity becomes negligible only for $T \gg T_D$. Inverse wavelength has been used for the independent axis so that a direct comparison with Varshni's original study [25] can be made.

4.2. Radiative properties

4.2.1. Spectral thermophysical emissivity and reflectivity

The range of validity for the model is based on the data from which it was regressed, and includes temperatures on the approximate range $[0, 1400]$ K and wavelengths on the approximate range $[1.5, 16]$ μm. A suitable candidate for baseline comparison with the proposed model cannot be found in the literature at the time of writing. This is due, in part, to the multiple properties for which the proposed model is capable of providing meaningful estimates. Models that do exist for independently achieving these estimates tend also to be defined over more limited spectral and temperature ranges than those investigated here. However, for assessment of the emissivity model, we can use the temperature-dependent normal spectral emissivity correlation first described by Edwards and Bayard de Volo in [35] and later refined by Edwards in [36]. We refer to this as the EBdV correlation. A comparison is drawn between the EBdV correlation and the proposed model in Fig. 5. The associated error metrics are provided in Table 2.

Since the parameters for the EBdV correlation were obtained by the authors of that study directly from the measurements at $T = \{306, 556, 833\}$ K, we expect their model to provide a competitive baseline, at the very least, for those measurements. This is the behavior that is more or less observed, with the proposed model yielding a better fit to six out of the eight total sets. The plots reveal that the most substantial contribution to the accumulated error of the EBdV model occurs in two regimes: (i) at small wavelengths for all temperatures, and (ii) at long wavelengths for low temperatures.

Error accumulation in (i) is due to the artificial imposition of an X-point—a wavelength λ_X such that $\epsilon(\lambda_X, T)$ does not vary with temperature. No such point exists for platinum on the given band

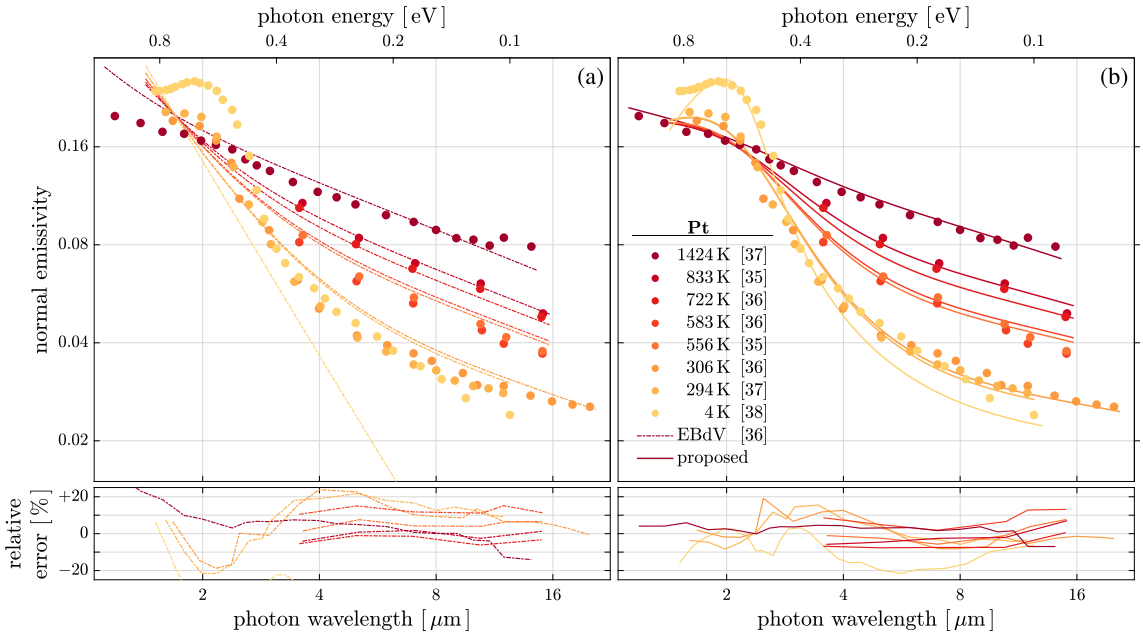

Fig. 5. Comparative fidelity of normal spectral emissivity models. Lines indicate models and markers indicate data. In plot (a): EBdV correlation [36]. In plot (b): the proposed model obtained by combining (1), (3), and (13) with the accessory Eqs. (10), (21), and (24) under the constraints (8) and (23) with the parameters in Table 1, and with use of Fresnel theory. To generate the normal emissivity, θ_i is set to zero. The corresponding bulk error metrics are provided in Table 2. The real-valued EBdV normal emissivity correlation provides a baseline for comparative assessment. The proposed model is capable of yielding estimates of greater complexity—as discussed in Section 4.2.2—since it retains complex-valued phase information.

Table 2
Comparison of modeling error for the temperature-dependent emissivity models in the plots of Fig. 5.

	Mean absolute relative error [%]							
	4 K	294 K	306 K	556 K	583 K	722 K	833 K	1424 K
EBdV [36]	38.9	13.5	10.4	5.0	12.5	3.5	2.1	8.4
Proposed	8.7	6.0	5.4	3.7	8.0	6.0	4.4	3.3

(the reader is directed to our earlier study [15] for a more detailed discussion on modeling with X-points which is based on the previous works of Winsemius [24]). Error accumulation in (ii) is due to the fact that the EBdV correlation does not account for the residual resistivity present in all real materials. In any case, we have used the EBdV correlation here mainly for its baseline illustrative purposes, since the proposed model is additionally capable of producing estimates for the complex-valued optical properties in addition to the real-valued emissivity.

In Fig. 6, we have plotted the surface generated by the spectral thermophysical normal reflectivity model along with the experimental data that was used to develop the model. One observes that for $T \gg T_D$, the emissivity is approximately invariant with changes in temperature along the band $\lambda \in [1.5, 3]$ μm, a result that is consistent with findings in the recent literature [48]. This can also be observed in Fig. 5(b). At higher temperatures, the effect of the interband component on the profile shape is smoothed. For $T \ll T_D$, the interband component is the dominant factor in determining the profile shape for NIR wavelengths, leading to a deeper reflectively minimum. The room temperature profile (and data), due to its relative nearness to the Debye temperature (consult Fig. 2 inset), is intermediary to the temperature-asymptotic behaviors.

4.2.2. Directional and total Planck-weighted properties

The proposed model provides interpolated estimates of the normal emissivity for the approximate wavelength and temperature ranges of $\lambda \in [1.5, 16]$ μm and $T \in [0, 1400]$ K. That is, these are the ranges for which interpolated estimates between experimental data points can be formed (*i.e.*, unpopulated regions of the surface plot in Fig. 6). However, when computing finite-bandwidth-averaged or total-bandwidth-averaged values that are weighted by the Planck energy density distribution, the model can be reliably extrapolated to shorter and longer wavelengths than implied by the experimental data. To aid in this analysis, we have plotted the normal emissivity (realized with the proposed model) alongside the corresponding Planck distribution

$$E_b(\lambda, T) = \frac{C_1}{\lambda^5 [\exp(C_2/\lambda T) - 1]}, \tag{25}$$

for five representative temperatures $T \in \{125, 250, 500, 1000, 2000\}$ K in Fig. 7. These values were chosen to represent the pre-transition range of platinum, with transition occurring at $T = 2041$ K. The first and second radiation constants in the Planck distribution are $C_1 = 2\pi h_p c_0^2$ and $C_2 = h_p c_0 / k_b$, respectively, where h_p is Planck's constant and k_b is Boltzmann's constant.

To establish the extrapolatory value of the model, we can consider the short and long wavelength regions separately. As can be inferred from Fig. 7, at wavelengths shorter than $\lambda \approx 0.25$ μm, the Planck distribution for all pre-transition temperatures applies a small weighting to the emissivity, so that this region is negligible. From 0.25 μm to 1.5 μm, the Planck weighting is non-negligible for pre-transition temperatures above roughly 1000 K. However, this also corresponds to temperatures for which the interband effects are smoothed, so that the model can be safely extrapolated to

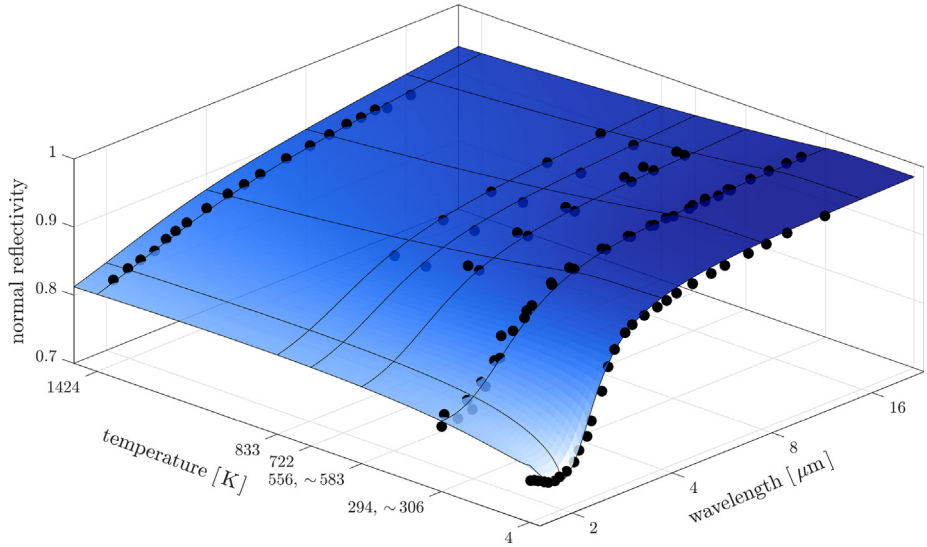

Fig. 6. Spectral thermophysical reflectivity. The surface is generated using the proposed model as described in the caption of Fig. 5. Markers indicate data corresponding to the values in that figure and the references are identified in its legend. The dominant feature at low temperatures is the reflectivity minimum at NIR wavelengths, which is primarily determined by the interband mechanism. At higher temperatures, this feature is smoothed due to the effects of temperature-dependent electron-phonon lattice coupling.

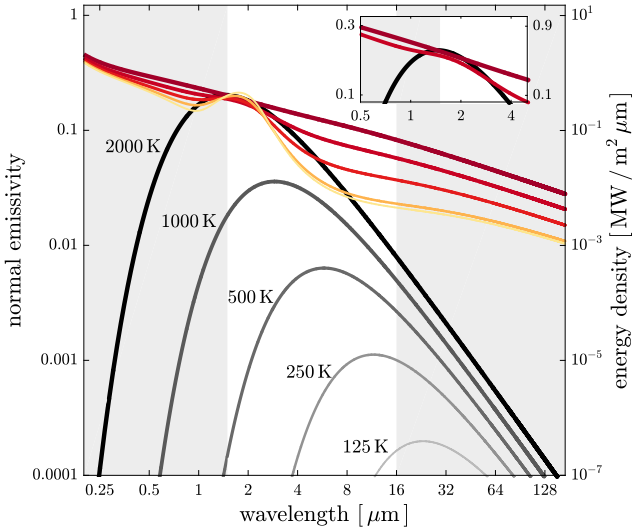

Fig. 7. Bandwidth-dependent effects of Planck-weighting for computation of total emissivity values. Labeled lines indicate Planck-distributions associated with the given temperature. Unlabeled lines indicate corresponding (from light to dark) normal emissivity profile. The white region indicates values interpolated by the model in terms of the experimental data. Grey regions indicate estimates that are extrapolated by the model beyond the experimental measurements.

the lower wavelength bound. This is more clearly illustrated in the inset of Fig. 7. At wavelengths above 16 μm, the Planck weighting is significant for all pre-transition temperatures above roughly 250 K. However, this also corresponds to the purely intraband region for which the response of the medium produces a Drude-like profile for all temperatures, with the emissivity approaching zero in a smooth, predictable manner as λ tends toward large values. Thus, the model can be safely extrapolated to the upper non-negligible bound $\lambda \approx 200$ μm.

The main takeaway of the foregoing analysis is that the model can be used for integration over the Planck distribution in order to determine total emissivity values at varying temperatures. The total directional emissivity at a given temperature is the integrated value

$$\epsilon_\theta(T,\theta_i) = \frac{1}{\sigma T^4}\int_0^\infty \epsilon(\lambda,T,\theta_i)E_b(\lambda,T)\,d\lambda, \tag{26}$$

where σ is the Stefan-Boltzmann constant and, in this context, θ_i is the polar emission angle. The total normal emissivity at a given temperature is then $\epsilon_\theta(T,0)$. Here we have let the emissivity be independent of the azimuthal emission angle ψ_i, an assumption that is valid for the specular (*i.e.*, optically smooth) media represented by the model. With this assumption in place, one can compute the spectral hemispherical emissivity:

$$\epsilon_\lambda(\lambda,T) = 2\int_0^{\pi/2} \epsilon(\lambda,T,\theta_i)\cos\theta_i \sin\theta_i\,d\theta_i, \tag{27}$$

from which the total hemispherical emissivity may then be obtained:

$$\epsilon(T) = \frac{1}{\sigma T^4}\int_0^\infty \epsilon_\lambda(\lambda,T)E_b(\lambda,T)\,d\lambda. \tag{28}$$

Fig. 8 demonstrates results for the total normal and total hemispherical emissivity computed from the proposed model alongside experimental values collected in two separate studies [49,50].

At first glance, it might appear that the model incorrectly predicts the values at higher temperatures, where a systematic deviation is observed between the model and the data. In fact, this is not the case and the deviation can be accounted for as follows. The definition for optical smoothness of a medium is a relative condition given by $e_{\text{rms}}/\lambda \ll 1$, where e_{rms} is the mean square roughness of the medium. For mechanically polished media such as that used to obtain the data on which the model was developed, $e_{\text{rms}} \sim 0.05$ μm. In other words, the modeled data is optically smooth throughout the important Planck-weighted bandwidth at any temperature.

However, for the studies represented in Fig. 8, the "smooth" samples were used as received without surface treatment, leading to $e_{\text{rms}} \sim 0.5$ μm. This means that the media are not smooth for $\lambda \lesssim 1$ μm, so that the spectral emissivity at these wavelengths will tend to be augmented (relative to an optically smooth sample). By inspection of Fig. 7, it is clear that this region will receive substantial weighting from Planck distributions corresponding to higher temperatures. As the temperature is increased, the peak of the distribution will be shifted more toward the non-smooth region, so

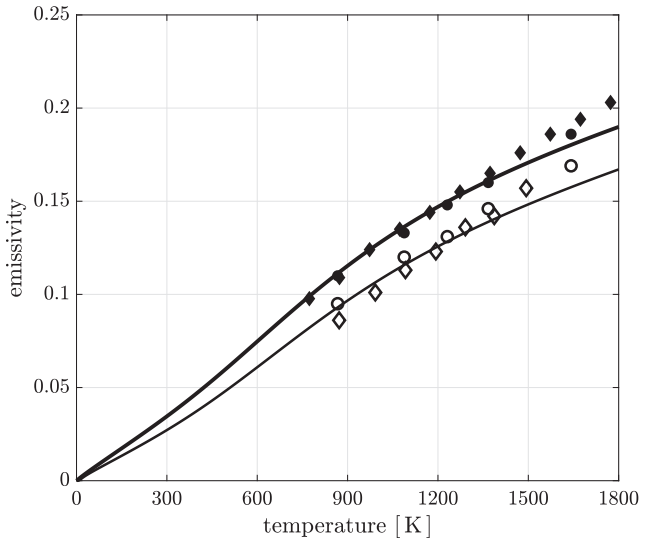

Fig. 8. Total normal and hemispherical emissivity of platinum. Lines: normal (thin) and hemispherical (thick) emissivity computed from the proposed model. Markers: normal (open) and hemispherical (filled) emissivity measurements taken from Ref. [49] (diamonds) and Ref. [50] (circles). The measurements were obtained with media that are optically smooth for $\lambda \gtrsim 1$ μm. For $\lambda \lesssim 1$ μm, these samples are not smooth and therefore have an augmented emissivity profile. As indicated in Fig. 7, this region is more heavily weighted at higher temperatures, leading to the associated deviations between the model and the data.

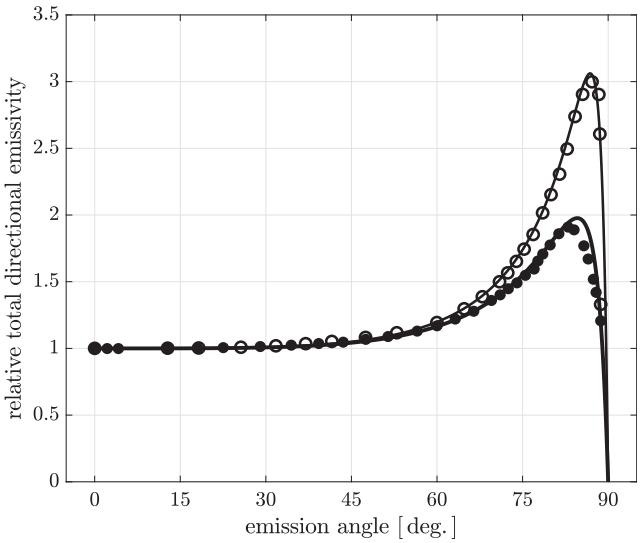

Fig. 9. Total directional emissivity of platinum. Lines: directional emissivity at $T = 865$ K (thin) and $T = 1645$ K (thick) computed from the proposed model. Markers: measurements at $T = 865$ K (open) and $T = 1645$ K (filled) taken from Ref. [50]. The model's accurate prediction of the profile shape, as well as the magnitude and location of the maximum indicates the validity of its use in conjunction with Fresnel theory. This, in turn, demonstrates the reliability of the extrapolated estimates of the complex-valued refractive index, which serves as an input to the Fresnel framework.

that the augmented emissivity is enhanced to a greater degree. This leads to precisely the deviations observed in Fig. 8. This effect is absent at lower temperatures, since the Planck weighting at lower temperatures suppresses the response at small wavelengths (see Fig. 7).

It is somewhat surprising that the deviations are not larger for the total hemispherical emissivity, since the roughened surface will tend to violate the specular assumption at smaller wavelengths. Indeed, it is stated in the noted studies that the roughness is directionally dependent, being somewhat greater in the direction of rolling (a result of the manufacturing process). Summarizing the main points of this analysis, the model represents smooth media at every temperature and, where the model and validation data agree, this is also true of the data. At higher temperatures, the deviations between the model and data signify the point beyond which the data do not represent values obtained for smooth media. This is an important observation, since more complicated frameworks that are developed, *e.g.*, to account for the effects of systematically or stochastically roughened surfaces often require optically smooth inputs. Non-smooth inputs to such frameworks are likely to yield spurious results.

Results for the relative total directional emissivity $\epsilon_\theta(T,\theta_i)/\epsilon_\theta(T,0)$ computed with the model at $T \in \{865, 1645\}$ K have been plotted alongside the data from Ref. [50] in Fig. 9. The results show that the model accurately predicts the profile shape, along with the magnitude and angle of the emissivity maximum (reflectivity minimum). The significance of this result is that the proposed model yields accurate estimates when coupled with Fresnel theory. Since the Fresnel theory requires, as an input, the complex-valued refractive index, this implies that the model has produced meaningful estimates of the refractive index at higher temperatures. This provides validation for the extrapolation (and inverse recovery) of the phase information from the real-valued emissivity (provided by the experimental data) as supported by the model structure. As discussed previously, such continuous estimates are often necessary for use with alternative Fresnel frameworks, such as those commonly used for the determination of the radiative properties of rough surfaces [51,52]. The lack of availability of measurements for the optical constants at various temperatures (both high and low) over the spectrally-resolved infrared regime can present a limitation for the development and analysis of such models.

5. Concluding remarks

The optical and radiative properties of metals in response to infrared radiative forcing play an important role in a number of theoretical and design-driven applications. In all but the most idealized scenarios the traditional Drude theory for modeling the intraband portion of this response fails to completely explain the experimental observations. A fundamental example is encountered in the nontrivial valencies of transition metals. The already-complicated issue of modeling the thermophysical properties of such media is further convoluted when interband dynamics represent a significant contribution to the infrared response.

To address these issues, we have expanded on our previous works by deriving a thermophysical model that accounts for the combined presence of anomalous intraband dynamics and interband dynamics activated at infrared wavelengths. The interband component represents an extension of our previous fixed-temperature model and provides an innovative temperature-dependent Gaussian-Lorentzian bound oscillator definition. The efficacy of the model has been demonstrated by applying it to platinum, a material possessing nontrivial valency and for which interband dynamics comprise a substantial portion of its infrared response. Application of the model is achieved by systematic regression of the model parameters from four distinct studies covering eight separate temperatures that span the range from far below to far above the Debye temperature.

The temperature-dependence of the intraband component has been imparted by a DC resistivity model possessing tunable low-temperature asymptotics. The resulting resistivity model agrees with direct measurements recorded elsewhere in the literature. Furthermore, we have shown that the temperature-dependence

of the resonant parameter for the bound oscillator definition—when taking into account both low- and high-temperature measurements—is appropriately described by a generalized Varshni-type empirical relation.

Results indicate that the proposed model is capable of producing accurate temperature-dependent directional spectral estimates of the surface radiative properties over the wavelength range $\lambda \in [1.5, 16]$ μm and over the temperature range $T \in [0, 1400]$ K. The results also show that when used to compute the total normal, directional, or hemispherical radiative properties, the proposed model can be accurately extrapolated over the entire Planck-weighted spectrum. The high degree of accuracy of the directional estimates validates the extrapolated estimation of the complex-valued refractive index (*i.e.*, inverse recovery of phase information). This important result demonstrates that the proposed model can be reliably interfaced with more complex Fresnel frameworks, such as those commonly employed for characterizing the properties of surfaces that have been systematically or stochastically roughened.

Declaration of Competing Interest

None.

Appendix A. Proof for non-causality of the convolution model

For the sake of simplicity and consistency, we will use the frequency-dependent form of the Efimov-Khitrov convolution, which is the form more commonly found in the literature. This is

$$\chi_{ek}(\omega) = \int_{-\infty}^{\infty} \mathcal{K}_g(y - \omega_n)\, \chi_l(\omega; y)\, dy, \tag{A.1}$$

where

$$\mathcal{K}_g(\omega_n) = \frac{1}{\sqrt{2\pi}\,\omega_\sigma} \exp\left[-\left(\frac{\omega_n}{\sqrt{2\pi}\,\omega_\sigma}\right)^2\right], \tag{A.2}$$

and

$$\chi_l(\omega; \omega_n) = \frac{\omega_p^2}{\omega_n^2 - \omega^2 - i\Gamma\omega}. \tag{A.3}$$

If the integral (A.1) diverges anywhere in its domain of integration, then it diverges completely. Thus, to prove non-causality we need only show that the integral diverges at any chosen point. In terms of the causality requirement established by the Kramers-Kronig relations (and assuming $\Gamma > 0$), the model is non-causal if it diverges at any point in the closed upper half complex plane. This process can be further simplified by separating the real and imaginary parts of this integral, and then showing that any one of these respective components diverges. To this end, we consider the real-part component

$$\mathcal{I}_f(\omega) = \int_0^1 f(y)\, dy, \tag{A.4}$$

where

$$f(y) = \frac{\exp[-(y-1)^2]\, y^2}{(y^2 - \omega^2)^2 + \Gamma^2\omega^2}, \tag{A.5}$$

and where we have taken $\omega_\sigma = 1/\sqrt{2\pi}, \omega_p = 1$, and $\omega_n = 1$ without loss of generality. We will show that $\lim_{\omega \downarrow 0} \mathcal{I}_f(\omega) \to \infty$, which implies that (A.1) diverges at $\omega = 0$ and is therefore non-causal. This can be achieved with a comparison test. We choose for our comparison function

$$g(y) = \frac{y^3}{(y^2 - \omega^2)^2 + \Gamma^2\omega^2}. \tag{A.6}$$

The comparison test is established by noting that if $f(y) \geqslant g(y)$ for all $y \in [0, 1]$, and if

$$\mathcal{I}_g(\omega) = \int_0^1 g(y)\, dy, \tag{A.7}$$

diverges to ∞, then $\mathcal{I}_f(\omega)$ also diverges. Defining

$$\begin{aligned} \Delta(y) &= f(y) - g(y), \\ &= \frac{[\exp[-(y-1)^2] - y]\, y^2}{(y^2 - \omega^2)^2 + \Gamma^2\omega^2}, \end{aligned} \tag{A.8}$$

it is straightforward to show by considering the numerator and denominator separately that $\Delta(y) > 0$ for all $y \in (0, 1)$. For $y \in \{0, 1\}, f(y) = g(y)$. Thus, $g(y)$ is a valid comparison function. We can now evaluate (A.7):

$$\begin{aligned} \mathcal{I}_g(\omega) = \frac{1}{4\Gamma}\Bigg[2\omega\left(\arctan\frac{\omega}{\Gamma} + \arctan\frac{1-\omega^2}{\Gamma\omega}\right) \\ + \Gamma\left[\ln(1 + (\Gamma^2 - 2)\omega^2 + \omega^4) - \ln(\omega^2(\Gamma^2 + \omega^2))\right]\Bigg]. \end{aligned} \tag{A.9}$$

We consider two limiting cases. First note that

$$\lim_{\Gamma \downarrow 0} \mathcal{I}_g(\omega \neq 0) \to \infty, \tag{A.10}$$

which is just a restatement of the fact that Γ must be nonzero to ensure causality ($\Gamma > 0$ for upper half plane analyticity). Physically, this is tantamount to the statement that the system must consist of nonzero dissipative forces. Finally, note that for $\Gamma > 0$,

$$\lim_{\omega \downarrow 0} \mathcal{I}_g(\omega) \to \infty, \tag{A.11}$$

which establishes the result we sought.

Appendix B. Composite emissivity models from fits to high temperature DC measurements

In Table 3 we have listed the bulk error metrics that result from using the proposed model structure and substituting the high-temperature (*i.e.*, $T > 294$ K) resistivity model with polynomial fits taken from the literature [45,46]. The polynomial fits were obtained by regression of direct DC measurements and yield a goodness of fit that is within the stated experimental uncertainty for each study. The expressions are not formally derived on the basis physical principles, and are therefore only valid over restricted temperature ranges. The fit of White is valid for $T \in [100, 2041]$ K, with the upper bound being the melting point of platinum. The fit of Wilthan has a stated range of validity $T \in [473, 1600]$ K, though it is clear by inspection of Fig. 2 that the two fits find excellent agreement below 473 K.

Table 3
Bulk error metrics for composite models. Composite A uses the ninth-order polynomial fit of White [45]. Composite B uses the second-order polynomial fit of Wilthan [46]. For each expression, the goodness of fit is within the experimental uncertainty associated with the discrete measured values.

	Mean absolute relative error [%]						
	294 K	306 K	556 K	583 K	722 K	833 K	1424 K
Composite A	7.2	7.2	3.6	8.4	5.5	3.8	2.8
Composite B	6.9	6.8	3.6	10.4	4.5	3.5	3.9

Appendix C. Supplementary material

Supplementary data associated with this article can be found, in the online version, at https://doi.org/10.1016/j.ijheatmasstransfer.2019.118471.

References

[1] D.J. Shelton, T. Sun, J.C. Ginn, K.R. Coffey, G.D. Boreman, Relaxation time effects on dynamic conductivity of alloyed metallic thin films in the infrared band, J. Appl. Phys. 104 (10) (2008) 103514, https://doi.org/10.1063/1.3026717.

[2] H. Kocer, S. Butun, Z. Li, K. Aydin, Reduced near-infrared absorption using ultra-thin lossy metals in Fabry-Perot cavities, Sci. Rep. 5 (2015) 8157, https://doi.org/10.1038/srep08157.

[3] G. Teodorescu, P.D. Jones, R.A. Overfelt, B. Guo, Normal emissivity of high-purity nickel at temperatures between 1440 and 1605K, J. Phys. Chem. Solids 69 (1) (2008) 133–138, https://doi.org/10.1016/j.jpcs.2007.08.047.

[4] C.-D. Wen, Investigation of steel emissivity behaviors: examination of Multispectral Radiation Thermometry (MRT) emissivity models, Int. J. Heat Mass Tran. 53 (9) (2010) 2035–2043, https://doi.org/10.1016/j.ijheatmasstransfer.2009.12.053.

[5] W. Zhu, D. Shi, Z. Zhu, J. Sun, Spectral emissivity model of steel 309S during the growth of oxide layer at 800–1100 K, Int. J. Heat Mass Tran. 109 (2017) 853–861, https://doi.org/10.1016/j.ijheatmasstransfer.2017.02.062.

[6] R.S. Hoffmann, A. Seewald, P.S. Schneider, F.H.R. França, Inverse design of thermal systems with spectrally dependent emissivities, Int. J. Heat Mass Tran. 53 (5) (2010) 931–939, https://doi.org/10.1016/j.ijheatmasstransfer.2009.11.030.

[7] P. Drude, Optische Eigenschaften und Elektronentheorie, Ann. Phys. 319 (10) (1904) 936–961, https://doi.org/10.1002/andp.19043191004.

[8] S. Roberts, Interpretation of the optical properties of metal surfaces, Phys. Rev. 100 (6) (1955) 1667–1671, https://doi.org/10.1103/PhysRev. 100.1667.

[9] S.R. Nagel, S.E. Schnatterly, Frequency dependence of the Drude relaxation time in metal films, Phys. Rev. B 9 (4) (1974) 1299–1303, https://doi.org/10.1103/PhysRevB.9.1299.

[10] H. Schulz-Baldes, Anomalous Drude model, Phys. Rev. Lett. 78 (11) (1997) 2176–2179, https://doi.org/10.1103/PhysRevLett. 78.2176.

[11] H.U. Yang, J. D'Archangel, M.L. Sundheimer, E. Tucker, G.D. Boreman, M.B. Raschke, Optical dielectric function of silver, Phys. Rev. B. 91 (23) (2015) 235137, https://doi.org/10.1103/PhysRevB.91.235137.

[12] J. Orosco, C.F.M. Coimbra, On a causal dispersion model for the optical properties of metals, Appl. Opt. 57 (19) (2018) 5333–5347, https://doi.org/10.1364/AO.57.005333.

[13] J. Orosco, C.F.M. Coimbra, Anomalous carrier transport model for broadband infrared absorption in metals, Phys. Rev. B 98 (23) (2018) 235118, https://doi.org/10.1103/PhysRevB.98.235118.

[14] J. Orosco, C.F.M. Coimbra, Thermophysical Model for the Infrared Emissivity of Metals, in: AIAA SciTech 2019 Forum, American Institute of Aeronautics and Astronautics, 2019, p. 1280, https://doi.org/10.2514/6.2019-1280.

[15] J. Orosco, C.F.M. Coimbra, Temperature-dependent carrier transport: low-complexity model for the infrared optical and radiative properties of nickel, J. Appl. Phys. 125 (20) (2019) 205108, https://doi.org/10.1063/1.5091792.

[16] V. Rehn, V.O. Jones, Vacuum ultraviolet (VUV) and soft X-ray mirrors for synchrotron radiation, OE 17 (5) (1978) 175504, https://doi.org/10.1117/12.7972270.

[17] T. Koide, S. Sato, T. Shidara, M. Niwano, M. Yanagihara, A. Yamada, A. Fujimori, A. Mikuni, H. Kato, T. Miyahara, Investigation of carbon contamination of synchrotron radiation mirrors, Nucl. Instrum. Methods Phys. Res. Sect. A: Acceler., Spectrom., Detect. Assoc. Equip. 246 (1) (1986) 215–218, https://doi.org/10.1016/0168-9002(86)90077-X.

[18] M. Ryan, Platinum in next-generation materials for data storage, Platin. Met. Rev. 54 (4) (2010) 244–249, https://doi.org/10.1595/147106710X525263.

[19] A. Cowley, B. Woodward, A healthy future: platinum in medical applications, Platin. Met. Rev. 55 (2) (2011) 98–107, https://doi.org/10.1595/147106711X566816.

[20] D.D.M. Ferreira, A.C. Jakobsen, S. Massahi, F.E. Christensen, B. Shortt, J. Garnæs, A. Torras-Rosell, M. Krumrey, L. Cibik, S. Marggaf, X-ray mirror development and testing for the ATHENA mission, in: Proc. SPIE, Vol. 9905, 2016, p. 99055K. https://doi.org/10.1117/12.2232962.

[21] J. Orosco, C.F.M. Coimbra, Variable-order modeling of nonlocal emergence in many-body systems: application to radiative dispersion, Phys. Rev. E 98 (3) (2018) 032208, https://doi.org/10.1103/PhysRevE.98.032208.

[22] M. Minissale, C. Pardanaud, R. Bisson, L. Gallais, The temperature dependence of optical properties of tungsten in the visible and near-infrared domains: an experimental and theoretical study, J. Phys. D: Appl. Phys. 50 (45) (2017) 455601, https://doi.org/10.1088/1361-6463/aa81f3.

[23] A. Yokozeki, D.J. Kasprzak, M.B. Shiflett, Thermal effect on C-H stretching vibrations of the imidazolium ring in ionic liquids, Phys. Chem. Chem. Phys. 9 (36) (2007) 5018–5026, https://doi.org/10.1039/B706497G.

[24] P. Winsemius, Temperature Dependence of the Optical Properties of Au and Ag Ph.D. thesis, Leiden University, 1973.

[25] Y.P. Varshni, Temperature dependence of the energy gap in semiconductors, Physica 34 (1) (1967) 149–154, https://doi.org/10.1016/0031-8914(67)90062-6.

[26] A.M. Efimov, V.N. Khitrov, Analytical formulas for describing the dispersion of glass with refractive indices that observe the continuous nature of absorption, Fiz. Khim. Stekla 5 (5) (1979) 583–588 (in Russian).

[27] R. Brendel, D. Bormann, An infrared dielectric function model for amorphous solids, J. Appl. Phys. 71 (1) (1992) 1–6, https://doi.org/10.1063/1.350737.

[28] J. Kischkat, S. Peters, B. Gruska, M. Semtsiv, M. Chashnikova, M. Klinkmüller, O. Fedosenko, S. Machulik, A. Aleksandrova, G. Monastyrskyi, Y. Flores, W.T. Masselink, Mid-infrared optical properties of thin films of aluminum oxide, titanium dioxide, silicon dioxide, aluminum nitride, and silicon nitride, Appl. Opt. 51 (28) (2012) 6789–6798, https://doi.org/10.1364/AO.51.006789.

[29] P. Jahanshahi, M. Ghomeishi, F.R.M. Adikan, Study on dielectric function models for surface plasmon resonance structure, Sci. World J. 2014 (2014) 503749, https://doi.org/10.1155/2014/503749.

[30] S. Nordebo, G. Kristensson, M. Mirmoosa, S. Tretyakov, Optimal plasmonic multipole resonances of a sphere in lossy media, Phys. Rev. B 99 (5) (2019) 054301, https://doi.org/10.1103/PhysRevB.99.054301.

[31] M. Abramowitz, I.A. Stegun, Handbook of Mathematical Functions with Formulas, Graphs, and Mathematical Tables, no. 55 in Applied Mathematics Series, U.S. Govt. Print. Off, Washington, 1972.

[32] A.D. Rakić, A.B. Djurišić, J.M. Elazar, M.L. Majewski, Optical properties of metallic films for vertical-cavity optoelectronic devices, Appl. Opt. 37 (22) (1998) 5271–5283, https://doi.org/10.1364/AO.37.005271.

[33] J. Orosco, C.F.M. Coimbra, Optical response of thin amorphous films to infrared radiation, Phys. Rev. B 97 (9) (2018) 094301, https://doi.org/10.1103/PhysRevB.97.094301.

[34] S.G. Johnson, Faddeeva Package, Massachusetts Institute of Technology, May 2015.

[35] D.K. Edwards, N. Bayard de Volo, Useful Approximations for the Spectral and Total Emissivity of Smooth Bare Metals, in: S. Gratch (Ed.), Advances in Thermophysical Properties at Extreme Temperatures and Pressures, ASME, New York, 1965, pp. 174–188.

[36] D.K. Edwards, Radiative transfer characteristics of materials, J. Heat Transf. 91 (1) (1969) 1–15, https://doi.org/10.1115/1.3580108.

[37] R.A. Seban, The emissivity of transition metals in the infrared, J. Heat Transf. 87 (2) (1965) 173–176, https://doi.org/10.1115/1.3689067.

[38] J.H. Weaver, Optical properties of Rh, Pd, Ir, and Pt, Phys. Rev. B 11 (4) (1975) 1416–1425, https://doi.org/10.1103/PhysRevB.11.1416.

[39] G.K. White, S.B. Woods, Electrical and thermal resistivity of the transition elements at low temperatures, Philos. T. Roy. Soc. A 251 (995) (1959) 273–302, https://doi.org/10.1098/rsta.1959.0004.

[40] R.N. Gurzhi, Mutual electron correlations in metal optics, Sov. Phys. JETP 8 (4) (1959) 673–675.

[41] S. Kasap, C. Koughia, H. Ruda, R. Johanson, Electrical Conduction in Metals and Semiconductors, in: S. Kasap, P. Capper (Eds.), Springer Handbook of Electronic and Photonic Materials, Springer US, Boston, MA, 2007, pp. 19–45, https://doi.org/10.1007/978-0-387-29185-7_2.

[42] E.N. Adams, Vasileff's calculation of electronic self-energy in semiconductors, Phys. Rev. 107 (3) (1957) 671, https://doi.org/10.1103/PhysRev. 107.671.

[43] P. Winsemius, F.F. van Kampen, H.P. Lengkeek, C.G. van Went, Temperature dependence of the optical properties of Au, Ag and Cu, J. Phys. F: Met. Phys. 6 (8) (1976) 1583–1606, https://doi.org/10.1088/0305-4608/6/8/017.

[44] M.Q. Brewster, Thermal Radiative Transfer and Properties, J. Wiley & Sons, New York, 1992.

[45] G.K. White, Recommended Values of Electrical Resistivity and Thermal Conductivity of Platinum, in: J.G. Hust (Ed.), Thermal Conductivity 17, Plenum Press, Gaithersburg, MD, 1981, pp. 95–104.

[46] B. Wilthan, C. Cagran, C. Brunner, G. Pottlacher, Thermophysical properties of solid and liquid platinum, Thermochim. Acta 415 (1) (2004) 47–54, https://doi.org/10.1016/j.tca.2003.06.003.

[47] L. Abadlia, F. Gasser, K. Khalouk, M. Mayoufi, J.G. Gasser, New experimental methodology, setup and LabView program for accurate absolute thermoelectric power and electrical resistivity measurements between 25 and 1600 K: application to pure copper, platinum, tungsten, and nickel at very high temperatures, Rev. Sci. Instrum. 85 (9) (2014) 095121, https://doi.org/10.1063/1.4896046.

[48] S. Deemyad, I.F. Silvera, Temperature dependence of the emissivity of platinum in the IR, Rev. Sci. Instrum. 79 (8) (2008) 086105, https://doi.org/10.1063/1.2966394.

[49] G.L. Abbott, N.J. Alvares, W.J. Parker, Total normal and total hemispherical emittance of polished metals, Part II, Tech. Rep. WADD-TR-61-94, Part II, Air Force Systems Command, Wright-Patterson Air Force Base, Ohio, Jan. 1963.

[50] R.E. Rolling, A.I. Funai, Investigation of the effect of surface conditions on the radiant properties of metals, Part II, Tech. Rep. AFML-TR-64-363, Part II, Air Force Systems Command, Wright-Patterson Air Force Base, Ohio, Apr. 1967.

[51] K. Tang, R.O. Buckius, A statistical model of wave scattering from random rough surfaces, Int. J. Heat Mass Tran. 44 (21) (2001) 4059–4073, https://doi.org/10.1016/S0017-9310(01)00050-3.

[52] J.L. King, H. Jo, S.K. Loyalka, R.V. Tompson, K. Sridharan, Computation of total hemispherical emissivity from directional spectral models, Int. J. Heat Mass Tran. 109 (2017) 894–906, https://doi.org/10.1016/j.ijheatmasstransfer.2017.01.120.